PCCP

PAPER

View Article Online
View Journal | View Issue

Cite this: *Phys. Chem. Chem. Phys.*, 2015, **17**, 21555

Temperature-dependent nanomorphology–performance relations in binary iridium complex blend films for organic light emitting diodes†

Young-Tae Kim,‡[a] Young-Hoon Kim,‡[a] Jae-Bok Seol,*[ab] Tae-Woo Lee[a] and Chan-Gyung Park[ab]

Received 14th June 2015,
Accepted 13th July 2015

DOI: 10.1039/c5cp03436a

www.rsc.org/pccp

Understanding the mechanism responsible for the temperature-dependent performances of emitting layers is essential for developing advanced phosphorescent organic light emitting diodes. We described the morphological evolution occurring in PVK:Ir(ppy)$_3$ binary blend films, with respect to thermal annealing up to 300 °C, by coupling atomic force microscopy and transmission electron microscopy. In particular, *in situ* temperature-dependent experimental characterization was performed to directly determine the overall sequence of morphological evolution occurring in the films. The device thermally annealed at 200 °C exhibits a noticeable enhancement in the performances, compared to the devices in the as-processed state and to the devices annealed at 300 °C. Our approaches reveal that the Ir(ppy)$_3$ molecules, with a needle-like structure in the as-processed state, were aggregated, and thus diffused into PVK without a morphological change at the temperature regime between 150 °C and 200 °C. Moreover, both network-like and droplet patterns existed in the devices annealed at 300 °C, which was beyond the glass temperature of PVK, leading to a profound increase in the surface roughness. The observed pattern formation is discussed in terms of viscoelastic phase separation. Based on our experimental findings, we propose that the performances of the devices are significantly controlled by the diffusion of dopant molecules and the morphological evolution of the host materials in binary blend systems.

Introduction

Organic light emitting diodes (OLEDs) have progressively received great attention for flat-panel display and illumination light source applications.[1] The pronounced manufacture of emitting layers in OLEDs with superior electrical properties has so far been achieved through vacuum-deposition and solution-processing. First, the vacuum-deposition process has been commercially performed as it promotes the efficiency of the devices. On the other hand, solution-processing has been introduced as a promising emerging manufacturing process, even though it provides a reduced efficiency of the devices compared to the former. This is due to the fact that the latter offers numerous feasible advantages, such as being an inexpensive process, producing a low amount of material waste, and the large-scale manufacturing for lightweight flexible devices is possible.[2–4] For enhancing the strategy of solution-processing with better performances, various techniques have systematically been considered *via* tailoring an optimal morphology which is beneficial for both charge transport and exciton confinement.[5] For instance, the chemical and electrical properties of polymer-based electroluminescent devices could be controlled by modifying the synthetic chemistry techniques of the emitting materials. Moreover, a more pronounced enhancement in the performances of devices was acquired by means of varying the processing conditions such as the solvent type, annealing treatment, and spin-coating speed during fabrication.[6–9] Among these strategies, the thermal annealing treatment has played an important role in easily controlling the device performance, as discussed previously.[10–16] The general interpretation of such annealing effects on the device is that an enhancement in the interfacial bonding between the substrate and the organic layers promotes the surface planarity of the organic films. As a result, electron–hole recombination is promoted. To better understand such a mechanism, atomic force microscopy (AFM) has been widely performed to reveal the correlations between the surface planarity and the device performance with respect to the thermal annealing treatment of OLEDs.[17–21]

[a] *Department of Material Science and Engineering, Pohang University of Science and Technology (POSTECH), Pohang 790-784, South Korea. E-mail: jb_seol@postech.ac.kr; Tel: +82 54 279 0220*
[b] *National Institute for Nanomaterials Technology (NINT), POSTECH, Pohang 790-784, South Korea*

† Electronic supplementary information (ESI) available. See DOI: 10.1039/c5cp03436a

‡ Authors contributed equally to this work.

Besides the surface planarity of the organic films, the distribution of guest and host components in the emitting layer during thermal annealing are also the governing microstructural components for developing efficient solution-processed OLEDs. Previous studies suggested that the aggregation of guest molecules yields the loss of luminescence efficiency due to their concentration quenching.[22–24] More recently, it was reported that a homogeneously distributed guest molecule in the host matrix was beneficial for an efficient energy transfer from the host to the guest molecules.[25,26] Consequently, the electron–hole recombination associated with the nanomorphology and distribution of the guest molecule is important in the enhancement in the performances of solution-processed OLEDs.[27–29] However, direct experimental evidence on the understanding of the microstructural components responsible for the temperature-dependent performances of organic-based devices is still lacking. To date, it has been a great challenge to tackle this issue due to a lack of *in situ* temperature-dependent experimental characterization. Therefore, a specific challenge for the *in situ* heating transmission electron microscopy (TEM) approach lies in characterizing the overall sequence of the microstructural evolution occurring in the emitting layer consisting of guest and host materials.

More specifically, this study aims at elucidating the pronounced correlations between the temperature-dependent device performance and the annealing-induced phenomena within the emitting layers. Here, we studied tris(2-phenylpyridine) iridium(III) ($Ir(ppy)_3$) blended into poly(*N*-vinyl carbazole) (namely PVK:$Ir(ppy)_3$ binary blend films), used for green emitting OLEDs.[30–32] Thus, we subject these materials to experimental approaches from *in situ* heating to *ex situ* annealing, placing a particular attention on the morphological change of both the PVK polymer and the $Ir(ppy)_3$ molecule, as well as on the associated concentration gradient of iridium. Based on our observation, an insight into the phase separation in the polymer blend film and into the diffusion of the guest molecules during thermal annealing will give us a better understanding of the relevant nanomorphology–performance correlations in phosphorescent OLEDs.

Experimental

PVK : $Ir(ppy)_3$ binary blend-based OLEDs were fabricated through solution-processing. Indium tin oxide (ITO) coated on glass was used as a substrate material. The surface of the glass was cleaned and treated through the following three steps; sonication in acetone and 2-isopropanol (IPA) for 15 min, followed by UV-ozone treatment for 10 min. Next, a hole injection layer (HIL) with a thickness of 40 nm was deposited by spin-coating. In particular, we used a HIL composed of a poly(3,4-ethylene dioxythiophene):polystyrene (sulfonic acid):tetrafluoroethylene-perfluoro-3,6-dioxa-4-methyl-7-octene-sulfonic acid copolymer (called PEDOT:PSS:PFI) for better electron–hole recombination.[32–35] Subsequently, it was transferred into the glove box after baking at 150 °C for 30 min prior to the fabrication of emitting layer, for the elimination of the solvent in the HIL. After baking, a PVK:$Ir(ppy)_3$ blend, diluted in chlorobenzene as a mixture with a PVK : $Ir(ppy)_3$ ratio of 10 : 1.5, was spin-coated at 2000 rpm for 90 s. In this study, PVK:$Ir(ppy)_3$ films with a thickness of 50 nm were deposited on the HIL. They were thermally annealed at 80, 150, 200, 250, and 300 °C for 60 min. After annealing, 1,3,5-tris(1-phenyl-1*H*-benzimidazol-2-yl)benzene (TPBI) with a thickness of 50 nm, 1 nm thick LiF, and 100 nm thick Al cathode layers were progressively deposited in the vacuum conditions of $<10^{-7}$ Torr for the fabrication of phosphorescent OLEDs. The thickness of the fabricated devices was determined though TEM characterization. Fig. 1 shows the chemical structures of

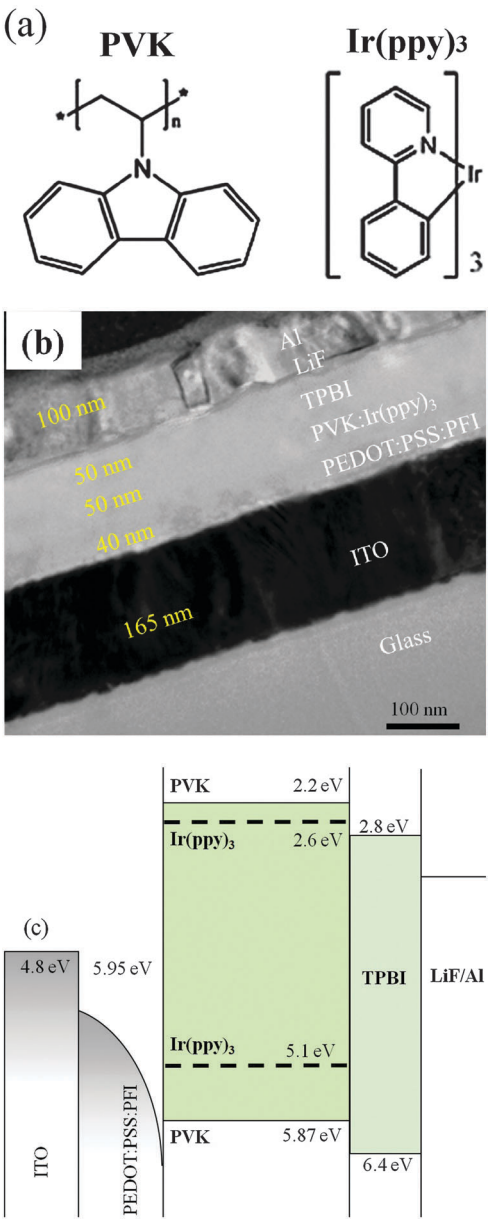

Fig. 1 (a) Chemical structures of the binary blend components, *i.e.* the guest $Ir(ppy)_3$ and host PVK materials, (b) TEM image showing the stacking structure of the OLED device containing PVK:$Ir(ppy)_3$ binary blend films, and (c) energy level diagram of the device fabricated in the present work.

the binary blend components used in this study, a TEM image of the overall stacking structure of the devices, and the corresponding energy level diagrams.

The electrical properties of the as-processed and thermally annealed devices were determined by their current density–voltage (J–V) characteristics with a sourcemeter (Keithley 236). The voltage (V)–luminance (L) characteristics were measured by a spectroradiometer (Minolta CS2000).

The samples for TEM observation were prepared by a floating method, prior to the deposition of an electron injection layer (EIL) and Al cathode layers. After fully dissolving the HIL of PEDOT:PSS:PFI in pure water, the PVK:Ir(ppy)$_3$ films floating on water were picked up by TEM mesh grids. The morphological evolution in the PVK:Ir(ppy)$_3$ binary blends occurring during thermal annealing was characterized by TEM (JEM 2010F) at an acceleration voltage of 200 kV. For measuring the iridium concentrations, energy dispersive X-ray spectrometry (EDS) of aberration-corrected scanning TEM (Cs-STEM) equipped with a high angle annular dark field (HAADF) detector was performed. In addition, the *in situ* temperature-dependent TEM approach was conducted with a heating specimen holder (GATAN). Using this approach, the nanomorphology of the PVK:Ir(ppy)$_3$ films was systematically observed with respect to the annealing temperature ranging from room temperature to 300 °C. In particular, we observed the time-dependent pattern evolution in the polymer at 300 °C for 300 s. During the *in situ* heating TEM experiments, the temperature was progressively controlled by heating with a step of 10 °C for every 1 min. The surface roughness of the PVK:Ir(ppy)$_3$ binary blends was determined by the AFM height and amplitude maps obtained in tapping mode.

Results and discussion

The performance of the present devices varies significantly with the applied annealing temperature ranging from room temperature to 300 °C. An enhanced current density is present in the device with the Ir(ppy)$_3$ doped PVK emitting layer annealed at 200 °C, and the device with the emitting layers annealed at 300 °C represents a substantial leakage current (Fig. 2a). The devices including the Ir(ppy)$_3$ doped PVK emitting layer in their as-processed state and annealed at 200 °C displayed an electro-luminescence (EL) peak at 512 nm corresponding to Ir(ppy)$_3$ molecules, showing a clear green emission (Fig. 2b). This implies that efficient energy transfer from the polymer host PVK to the Ir(ppy)$_3$ dopant molecules occurs for the as-processed devices and the devices annealed at 200 °C. On the other hand, the thermally annealed devices at 300 °C showed an emission peak at 412 nm arising from PVK. It reveals that the energy transfer from PVK to Ir(ppy)$_3$ was prohibited by annealing at 300 °C, and thus only blue light from PVK was emitted. The measured current efficiency and luminance of the devices annealed at 200 °C were ~14.6 cd A^{-1} and ~5000 cd m^{-2}, while they were ~3.8 cd A^{-1} and ~360 cd m^{-2} for the devices in the as-processed state and ~0.14 cd A^{-1} and ~130 cd m^{-2} for the devices annealed at 300 °C, respectively (Fig. 2b and c). A more profound enhancement in the efficiency and luminance of the devices annealed at 200 °C is likely to be responsible for an increase in the radiative electron–hole recombination. This means that better energy transfer from PVK to Ir(ppy)$_3$ and lower intermolecular quenching between Ir(ppy)$_3$ molecules can be achieved. Therefore, we found that the performances of the PVK:Ir(ppy)$_3$ binary blend-containing OLEDs significantly depend

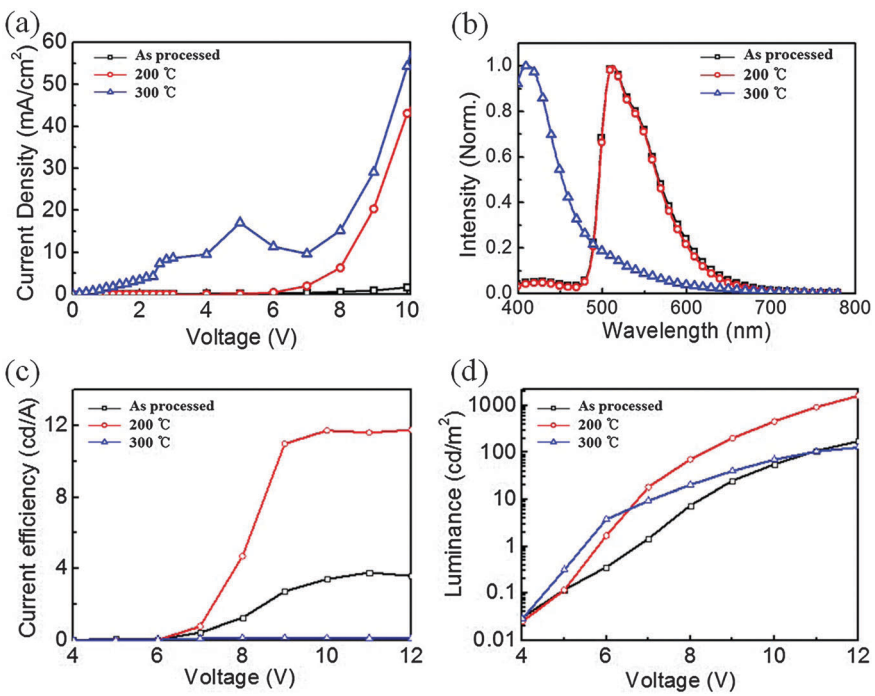

Fig. 2 Device performances of the PVK:Ir(ppy)$_3$ films with respect to thermal annealing: (a) current density, (b) EL spectra, (c) current efficiency, and (d) luminance. The blank rectangles, circles, and triangles represent the as-processed state, annealed at 200 °C and 300 °C, respectively.

on the temperature, ranging from room temperature to 300 °C. Moreover, this observation is analogous to the previous studies that an appropriate thermal annealing of the PVK:$Ir(ppy)_3$ films is favorable for better energy transfer of the solution-processed OLEDs.

So as to reveal the relations between the temperature-dependent performances and the nanostructure of the PVK:$Ir(ppy)_3$ binary blend films, *in situ* temperature-dependent TEM experiments were performed, as shown in Fig. 3. This approach enables us to directly provide the overall sequence of morphological evolution occurring in the film during thermal heating. Prior to the annealing treatment (called the as-processed state), a two-dimensional aggregation is homogeneously distributed in the polymer matrix (PVK), showing needle-like features with a high aspect ratio (a length of 1–2 μm, a width of 30–40 nm) as shown in Fig. 3a. The needles appear to be darker than that of the PVK matrix in the TEM images. It has been generally known that when using the bright-field mode of TEM, the contrast of regions with a higher atomic number appears to be darker due to larger electron scattering. Taking into account the higher atomic number of iridium than the components of PVK, the needle-type aggregations with a darker contrast are likely to be $Ir(ppy)_3$ molecules. With an increase in temperature up to 150 °C, the contrast at the corner of the needle-type $Ir(ppy)_3$ aggregations becomes gradually brighter compared to PVK. Namely, the bright and dark regions of the needle-type $Ir(ppy)_3$ molecules can be clearly distinguished, as marked with the arrows shown in Fig. 3c. This indicates that the local contrast variation of the $Ir(ppy)_3$ needles is promoted by thermal annealing, but within a limited temperature regime. Nevertheless, thermal annealing at 150 °C did not induce any important morphological evolution of the needles. The measured morphological parameters, such as the width and length of the needles, were constant. Around a higher temperature of 200 °C, the contrast of the $Ir(ppy)_3$ needles becomes fully bright, as shown in Fig. 3d. At 250 °C, which was above the glass-transition temperature (T_g) of PVK in the present case, the interface between the $Ir(ppy)_3$ molecules and the host materials is blurred and thus the needles disappear gradually. At the temperature of 300 °C, network-like patterns are present in the earlier state (Fig. 3f) and then circular particles are observed with a longer time (Fig. 3g and h). This means that during annealing at 300 °C, the network structure eventually transforms into droplet patterns or circular particles. The observed pattern evolution in the devices annealed at 300 °C agrees with previous experimental results and numerical simulations of polymer solutions.[36] Following this concept, we propose that thermal annealing above T_g can make polymer materials exhibit a fluid-like behavior, and hence movement of the polymer chains is activated. As a result, the polymer chains above T_g can become mobile and form the network structures as shown in Fig. 3(f)–(h). The contrast of the polymer regions is temporally getting darker, which means that the host PVK polymer aggregation becomes dense. After a while, the thin parts of the polymer aggregates are elongated and a droplet structure can be formed due to the elastic force balance instead of interfacial tension (Fig. 3h).[36] Based on our TEM results and those found in the literature, we consider that the observed spherical particles found in the films annealed at 300 °C are likely to be attributed to a polymer phase separation of PVK during thermal annealing. And hence, the energy transfer from the host to the guest could not occur efficiently due to the phase separation or the aggregation of the host PVK, resulting in the noticeable

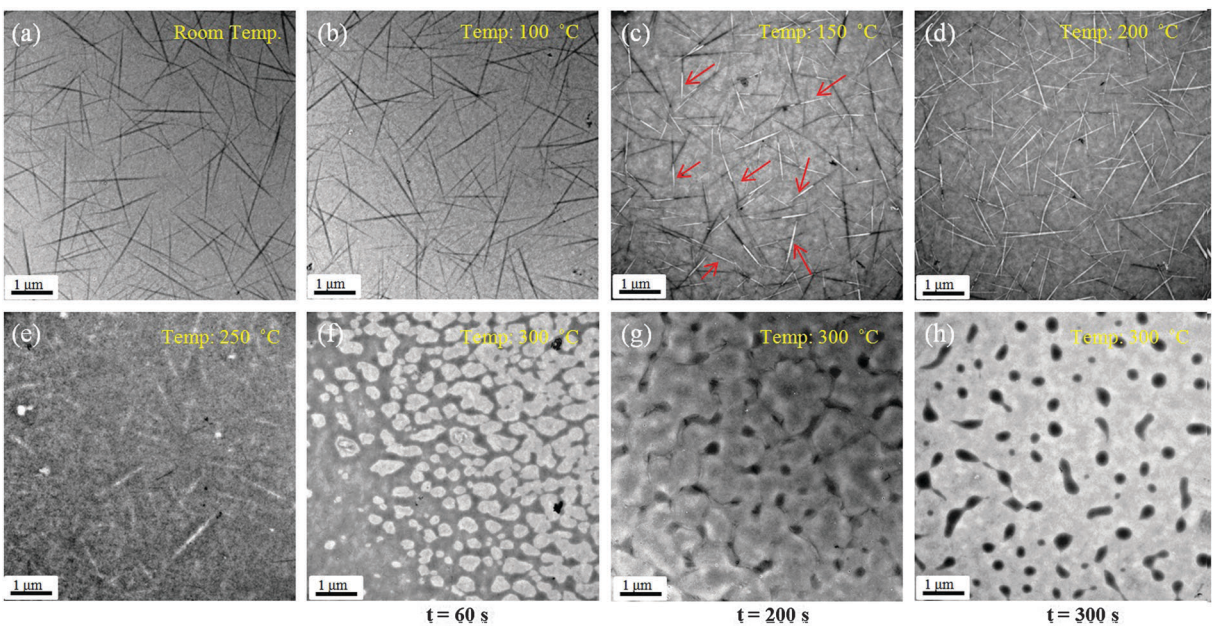

Fig. 3 Bright-field images observed by *in situ* temperature-dependent TEM experiments ranging from room temperature to 300 °C: (a) the as-processed PVK:$Ir(ppy)_3$ binary blend film, (b) 100 °C, (c) 150 °C, (d) 200 °C, (e) 250 °C, and (f) 300 °C, respectively. (g) and (h) The time-dependent pattern evolution occurring at 300 °C. Note that the local contrast changes of the needle-like features are shown within the limited temperature regime as marked with the arrows.

degradation of current efficiency and luminance for the devices annealed at 300 °C. Using *in situ* temperature-dependent TEM characterization, we found that the morphological or pattern evolution is an important factor contributing to the device performances of solution-processed PVK:Ir(ppy)$_3$ binary blend films. Further detailed information of the circular particles observed at the devices annealed at 300 °C is discussed in the next section.

More specific attention is paid to the origin of the needle-type aggregations observed in the as-processed devices, and to the local contrast changes in the devices thermally annealed at 150 °C as well as to the circular particles in the device annealed at 300 °C. To resolve these issues, the EDS and HAADF techniques of *ex situ* (S)TEM analysis were performed. The EDS results revealed that the concentration of iridium atoms along the direction (marked with the arrows) across the interfaces between the needles and PVK significantly varies with the applied annealing temperature, as shown in Fig. 4. In the as-processed state, a two-dimensional nanostructure with needle-type morphology

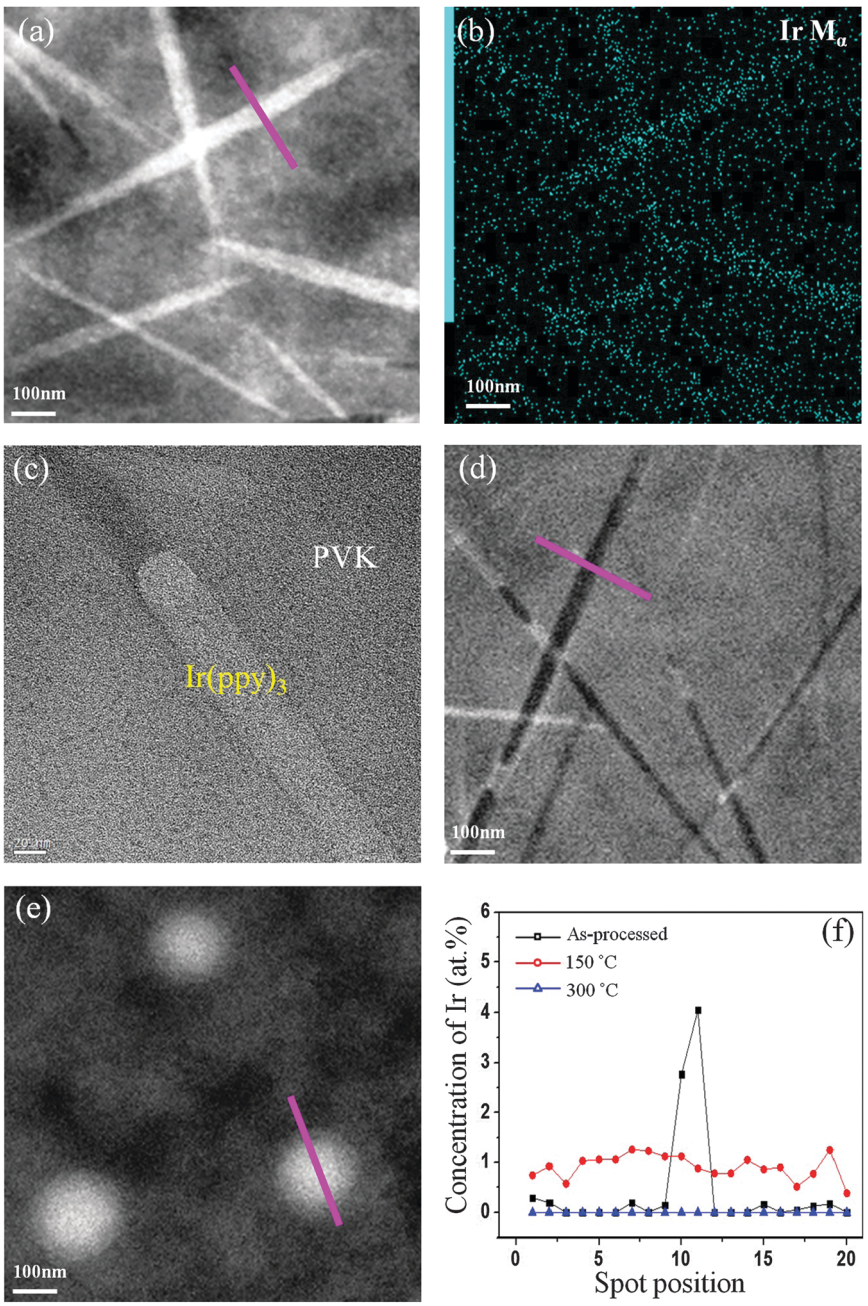

Fig. 4 (a) HAADF-STEM image taken from the as-processed PVK:Ir(ppy)$_3$ binary blend films and (b) the corresponding enlarged EDS elemental map of Ir (M$_\alpha$). (c) The high-resolution (S)TEM image of the film annealed at 150 °C. HAADF-STEM images of the film thermally annealed at (d) 150 °C and (e) 300 °C, respectively. (f) The corresponding 1-D concentration profiles of Ir along the direction (marked with the arrows taken from ROI) across the interfaces between the needles and PVK. The rectangles, circles, and triangles represent the as-processed state, annealed at 150 °C and 300 °C, respectively.

is visible (Fig. 4a). This is in good accordance with the *in situ* heating TEM experiments shown in Fig. 2a. Generally, the contrast shown in the HAADF image is reversed to that of the bright-field mode of TEM, *i.e.*, a heavier element contributes to a brighter contrast. Fig. 4b displays the corresponding EDS mapping of the iridium atoms, revealing that the observed needle-like features are unambiguously $Ir(ppy)_3$ molecules. Here, the intensity-profiles of 1.977 eV corresponding to Ir-M_α signals were acquired from the needle-like features. We demonstrate that the aggregation of $Ir(ppy)_3$ found in the as-processed devices introduces inefficient energy transfer and severe exciton quenching, leading to the degraded performance of the devices (Fig. 2). The origin of the needle-like features of the guest molecules was systematically revealed in earlier studies.[37–39] For instance, the needle-like aggregation of EPPTC molecules embedded in a PFO film could be formed through π-stacking during a spin-coating process.[37] Similarly, Liu *et al.*[38] proved from the result of X-ray diffraction (XRD) that the π-stacking interaction in the solid state played an important role in a highly ordered extended aggregation morphology of conjugated molecular systems. More recently, Salim *et al.*[39] suggested that the observation of needle-type $Ir(ppy)_3$ aggregates in ternary blend films was an indicator of the ability of the $Ir(ppy)_3$ molecules to self-assemble into nanostructures, even under spin-coating. Therefore, we propose that the formation of the needle-like $Ir(ppy)_3$ aggregates in the PVK:$Ir(ppy)_3$ binary system at room temperature (namely the as-processed state) is likely to be ascribed to their self-assembly during solvent evaporation in the fabrication of solution-processed OLEDs. Additionally, our TEM observation of needle-type $Ir(ppy)_3$ molecules in the PVK:$Ir(ppy)_3$ binary system has not been introduced to date, except for $Ir(ppy)_3$ molecules in P3HT, PF, and PFHP films.[38–41]

The high-resolution (S)TEM and HAADF images taken from the thermally annealed films at 150 °C show a local contrast variation of the $Ir(ppy)_3$ needles, which is promoted by thermal annealing (Fig. 4c and d). This agrees with the results acquired through the *in situ* heating TEM approach, as shown in Fig. 3c. Although the experimental pressure during the *in situ* heating approach is much lower compared to *ex situ* thermal annealing, the temperature difference of the two approaches was not efficient in this study. From this TEM observation, we found that the noticeable enhancement in the emitting efficiency of the devices annealed at 200 °C (Fig. 2) is substantially attributed to the contrast changes of the needle-type $Ir(ppy)_3$ aggregation (see Fig. 3c, 4c and d). EDS analysis revealed the origin of the contrast change observed in the needles for the thermally annealed devices: it is the concentration gradient of $Ir(ppy)_3$

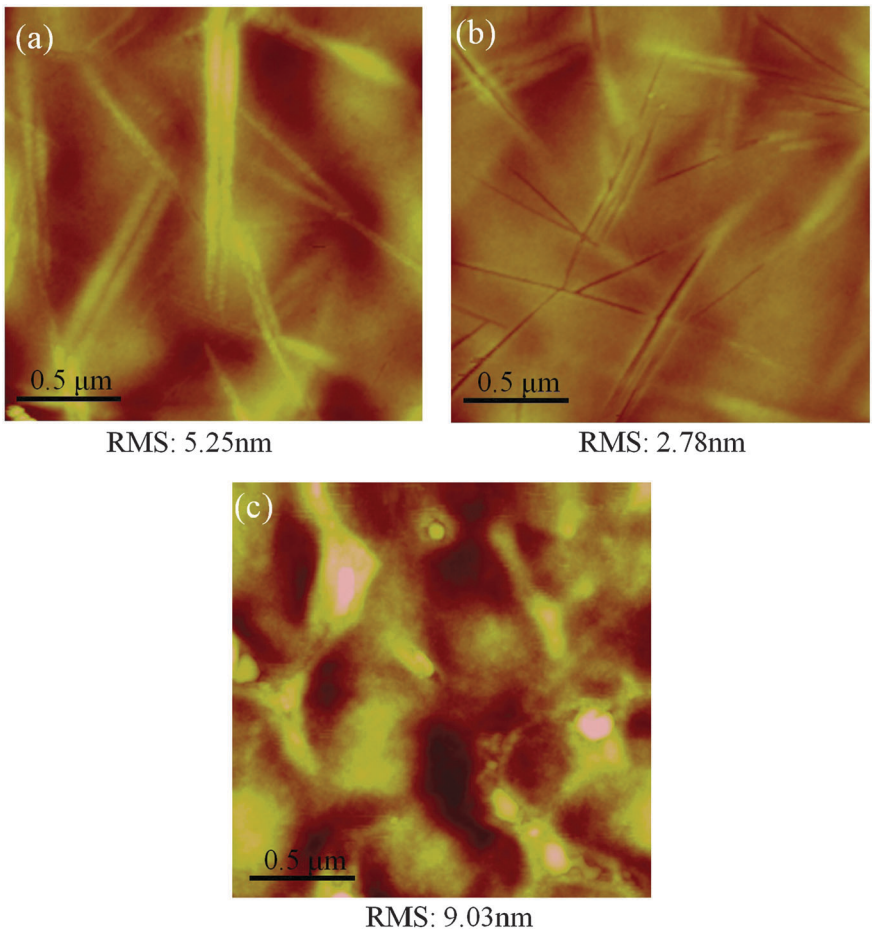

Fig. 5 Tapping mode AFM height images of (a) as-processed PVK:$Ir(ppy)_3$ binary blend films, and films thermally annealed at (b) 150 °C and (c) 300 °C, respectively.

molecules that occurred during thermal annealing. Clearly, the distribution of iridium atoms along the direction (marked with the arrows) across the interfaces between the needles and PVK is homogeneous, as represented by the red line in Fig. 4f. Moreover, the Ir-M_α peak of 1.977 eV and the Ir-L_α peaks of 9.174 eV were strongly detected at the brighter regions in the HAADF image as shown in Fig. S1 of the ESI†. Thus, we did not detect any remarkable concentration disparity of carbon and nitrogen between the matrix and the needle region, regardless of the annealing temperature. Considering that $Ir(ppy)_3$ molecules mainly consist of carbon and nitrogen, it is plausible that the observed concentration gradient of the needle-type $Ir(ppy)_3$ molecules in the devices annealed at a temperature ranging between 150 °C and 200 °C is induced not by the decomposition of iridium and carbon atoms separately, but by the diffusion of the $Ir(ppy)_3$ molecules themselves. This is due to the thermal stability of the $Ir(ppy)_3$ molecules below a temperature of 300 °C.[42] Based on our results, we suggest that the origin of a pronounced enhancement in the emitting performances of solution-processed OLEDs by up to three orders of magnitude is the diffusion of $Ir(ppy)_3$ molecules associated with an appropriate annealing temperature. Thus, we consider that an increase in the annealing temperature is likely to accelerate the mobility of the needle-type $Ir(ppy)_3$ aggregates themselves, leading to the diffusion of $Ir(ppy)_3$ into the PVK, sustaining the needle-like morphology. However, the exact kinetics of the $Ir(ppy)_3$ diffusion responsible for the material transport cannot be explained from a thermodynamic point of view, due to a lack of a database in the literature.

As the annealing temperature increases further, circular particles were displayed instead of needles. The observed circular particles in the emitting layer annealed at 300 °C are an indicator of the occurrence of the PVK:$Ir(ppy)_3$ pattern evolution during the annealing treatment. The $Ir(ppy)_3$ molecules in the emitting layer annealed at 300 °C are well distributed into the PVK matrix, as shown in Fig. 4f. Here, it is worth mentioning that the measured concentration of iridium along the direction marked with the arrows for the annealed samples at 300 °C is remarkably reduced compared to that for the films annealed at 200 °C (red line). The measured concentration of iridium in the emitting layer was below ~0.05 at% for the films annealed at 300 °C, as represented by the blue line in Fig. 4f. This result indicates that the spherical particles with a droplet pattern found in the films annealed at 300 °C are not $Ir(ppy)_3$ molecule aggregations, but are PVK aggregations. As mentioned previously, Tanaka[36] proposed that viscoelastic phase separation should be universal to any dynamically asymmetric mixtures, including polymer solutions consisting of fast and slow components, and thus viscoelastic effects significantly control the critical dynamics of polymer solutions or blends. Based on our TEM findings and those in the literature, we consider that viscoelastic phase separation is likely to be the mechanism responsible for the observed time-dependent pattern evolution of the polymers at 300 °C.

The concentration gradients and morphological evolution affect the surface uniformity of the binary blend films, as shown in Fig. 5. The surface roughness of the needle-type $Ir(ppy)_3$ aggregations with a high aspect ratio was 5.25 nm in the as-processed films. Meanwhile, thermal annealing up to 200 °C introduces the

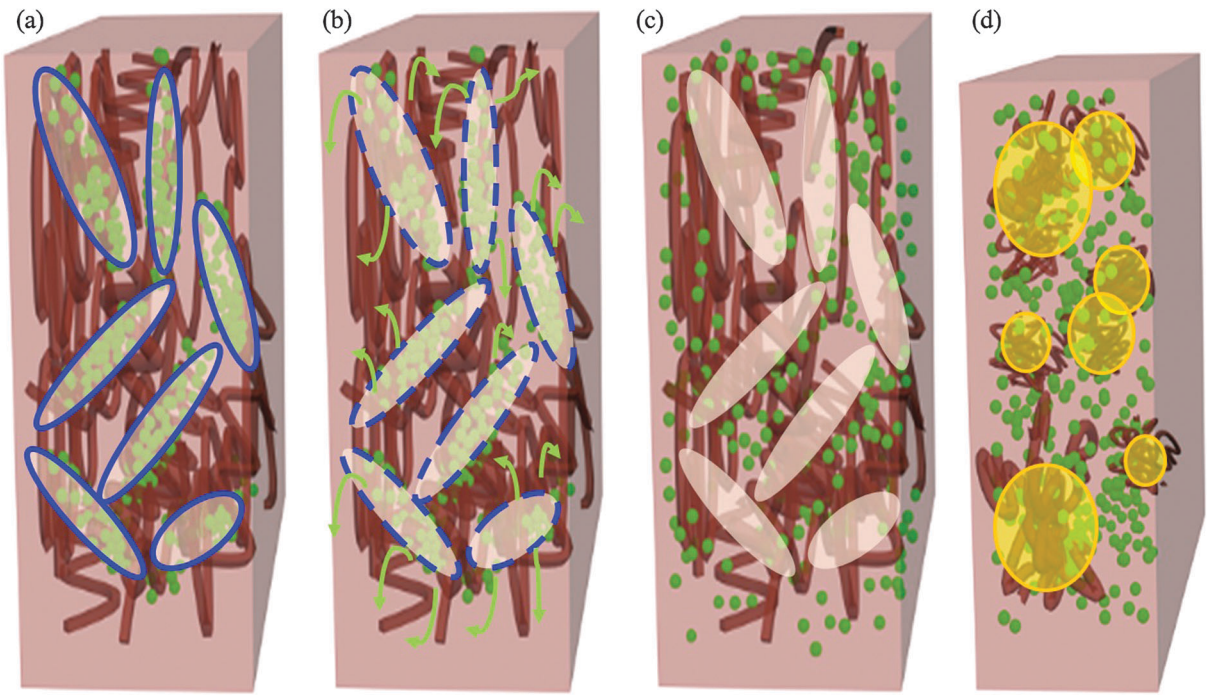

Fig. 6 Schematic illustrations showing the overall sequence of microstructural evolution occurring in the thermally annealed PVK:$Ir(ppy)_3$ binary blend system. The green dots, blue needles, and yellow circles represent $Ir(ppy)_3$, the aggregation of $Ir(ppy)_3$ molecules, and the droplet pattern of PVK, respectively. Note that at 300 °C the binary blend film shrinks, leading to a reduction of its volume.

enhanced surface uniformity. The measured surface roughness was 2.78 nm for the device annealed at 200 °C. With an increase in the annealing temperature up to 300 °C, the surface uniformity was dramatically degraded due to the presence of large spherical particles with a droplet pattern on the surface. The surface roughness was estimated at 9.03 nm.

By means of coupling the *in situ* temperature-dependent experimental and *ex situ* annealing approaches carried out in the present study, schematics are illustrated, as shown in Fig. 6. The schematic illustration can explain the overall sequence of microstructural evolution in the guest and host materials occurring during thermal annealing for the PVK:Ir(ppy)$_3$ binary blend system. In the as-processed state (Fig. 6a), the needle-like aggregation (blue) of Ir(ppy)$_3$ molecules (green dots) is distributed well in the PVK polymer (brown). With an increase in the temperature, the Ir(ppy)$_3$ molecules diffused into PVK, sustaining their original needle-like morphology, as indicated with the arrows (Fig. 6b). Subsequently, the Ir(ppy)$_3$ molecules exist in the PVK polymer, as shown in Fig. 6c. At 300 °C, the binary blend film shrinks and thus spherical particles with a droplet pattern (yellow) are formed in the films, resulting from the phase separation of PVK (Fig. 6d).

Conclusions

We investigated the temperature-dependent efficiency, morphological evolution and the dopant distribution of PVK:Ir(ppy)$_3$ binary blend emitting films with respect to the applied annealing temperature ranging from room temperature to 300 °C through *in situ* temperature-dependent TEM. Further analyses of AFM and (S)TEM-EDS confirmed the characteristics found by the *in situ* TEM experiments. They reveal that the diffusion of the Ir(ppy)$_3$ molecules and the phase separation of polymers are important in determining the device performances of solution-processed PVK:Ir(ppy)$_3$. The main conclusions derived from our experimental results are summarized below.

(1) Efficient energy transfer from PVK to Ir(ppy)$_3$ for the as-processed state and the devices at 180 °C is visible, whereas there is an absence of energy transfer for the devices annealed at 300 °C. In addition, a superior combination of efficiency and luminance is achieved for the device annealed at 200 °C, indicating a higher electron–hole recombination or better exciton confinement. As a result, the performances of the PVK:Ir(ppy)$_3$ binary blend-based OLEDs are significantly temperature-dependent in the range from room temperature to 300 °C.

(2) At a reference state, a two-dimensional nanostructure tends to form in the polymer films, showing needle-like features with a high aspect ratio. Using TEM-EDS, it is revealed that the Ir(ppy)$_3$ molecules are aggregated as needle-features in the PVK:Ir(ppy)$_3$ films, which was induced by the solvent evaporation in the fabrication of solution-processed OLEDs.

(3) During annealing at 200 °C, a chemical gradient of Ir(ppy)$_3$ molecules occurs while their original needle-type morphology, formed initially in the as-processed state, is sustained. In addition, we demonstrated that, using a quantitative analysis across the boundaries between the Ir(ppy)$_3$ aggregations and the PVK matrix, thermal annealing at 200 °C introduces a higher mobility of the Ir(ppy)$_3$ molecules and then leads to their diffusion into the host materials. Consequently, the surface uniformity is substantially improved. Therefore, the diffusion of Ir(ppy)$_3$ molecules, associated with an appropriate annealing temperature rather than the formation of their needle-like morphology, is responsible for the pronounced enhancement in the emitting performance of the solution-processed OLEDs.

(4) The devices annealed at much higher than the glass temperature of the host materials exhibited degraded efficiency and characteristics of phosphorescent emission. The observed network-like pattern and spherical particles with a droplet pattern in the films annealed at 300 °C are attributed to a polymer phase separation of PVK during annealing, leading to the pronounced degradation of the device performances. Here, viscoelastic phase separation is probably the mechanism underlying the pattern evolution.

Overall, the thermally annealed PVK:Ir(ppy)$_3$ binary blend emitting films presented in this work show good performances of current efficiency and luminance, rendering them suitable for applications in phosphorescent OLEDs. In addition, our experimental approaches proposed in this study can provide direct evidence of the relevant nanomorphology–performance correlations in various polymer-based OLEDs.

Acknowledgements

This work was financially supported by the National Research Foundation of Korea (NRF) grants funded by the Korean Government (MEST) (No. 2011-0020252).

References

1 C. W. Tang and S. A. Vanslyke, *Appl. Phys. Lett.*, 1987, **51**, 913.
2 H. Wu, G. Zhou, J. Zou, C. L. Ho, W. Y. Wong, W. Yang, J. Peng and Y. Cao, *Adv. Mater.*, 2009, **21**(41), 4181.
3 K. S. Yook, S. E. Jang, S. O. Jeon and J. Y. Lee, *Adv. Mater.*, 2010, **22**(40), 4479.
4 L. Duan, L. Hou, T.-W. Lee, J. Qiao, D. Zhang, G. Dong, L. Wang and Y. Qiu, *J. Mater. Chem.*, 2010, **20**, 6392.
5 J.-H. Jou, S. Kumar, A. Agrawal, T.-H. Li and S. Sahoo, *J. Mater. Chem. C*, 2015, **3**, 2974.
6 K. M. Vaeth and C. W. Tang, *J. Appl. Phys.*, 2002, **92**, 3447.
7 K. H. Yim, W. J. Doherty, W. R. Salaneck, C. E. Murphy, R. H. Friend and J. S. Kim, *Nano Lett.*, 2010, **10**, 385.
8 S. E. Shaheen, C. J. Brabec, N. S. Sariciftci, F. Padinger, T. Fromherz and J. C. hummelen, *Appl. Phys. Lett.*, 2001, **78**, 841.
9 Y. K. Kim, S. A. Choulis, J. Nelson, D. D. C. Bradley, S. Cook and J. R. Durrant, *Appl. Phys. Lett.*, 2005, **86**, 063502.
10 S. Caria, E. D. Como, M. Murgia, R. Zamboni, P. Melpiganano and V. Biondo, *J. Phys.: Condens. Matter*, 2006, **18**, S2139.
11 B. J. Chen, X. W. Sun and K. R. Sarma, *Mater. Sci. Eng., B*, 2007, **139**, 192–196.

12 G. Baldacchini, T. Baldacchini, P. Chiacchiaretta, R. B. Pode, M. A. Vincenti and Q.-M. Wang, *ECS Trans.*, 2009, **16**(31), 3.
13 M. Thomschke, S. Hofmann, S. Olthof, M. Anderson, H. Kleemann, M. Schober, B. Lussem and K. Leo, *Appl. Phys. Lett.*, 2011, **98**, 083304.
14 J. Liu, T. F. Guo and Y. Yang, *J. Appl. Phys.*, 2002, **91**(3), 1595.
15 J. H. Ahn, C. Wang, N. E. Widdowson, C. Pearson and M. R. Bryce, *J. Appl. Phys.*, 2005, **98**, 054508.
16 Y. H. Niu, Q. Hou and Y. Cao, *Appl. Phys. Lett.*, 2002, **81**, 634.
17 M. C. Sun, J. H. Jou, W. K. Weng and Y. S. Huang, *Thin Solid Films*, 2005, **491**, 260.
18 M. L. Tu, Y. K. Su, S. J. Chang, T. H. Fang, W. H. Chen and H. Yang, *Jpn. J. Appl. Phys.*, 2005, **44**(4B), 2787.
19 G. T. Chen, S. H. Su, C. C. Hou and M. Yokoyama, *J. Electrochem. Soc.*, 2007, **154**(5), J159.
20 T.-W. Lee and O. O. Park, *Adv. Mater.*, 2000, **12**(11), 801.
21 J. W. Kim, J. Y. Lee, C. W. Han, N. Y. Lee and I. J. Chung, *Appl. Phys. Lett.*, 2003, **82**, 24.
22 Y. Kawamura, J. Brooks, J. J. Brown, H. Sasabe and C. Adachi, *Phys. Rev. Lett.*, 2006, **96**, 017404.
23 J. R. Gong, L. J. Wan, S. B. Lei and C. L. Bai, *J. Phys. Chem. B*, 2005, **109**, 1675.
24 W. J. Shi, J. Barber and Y. Zhao, *J. Phys. Chem. B*, 2013, **117**, 3976.
25 J. H. Jou, W. B. Wang, S. Z. Chen, J. J. Shyue, M. F. Hsu, C. W. Lin, S. M. Shen, C. J. Wang, C. P. Liu, C. T. Chen, M. F. Wu and S. W. Liu, *J. Mater. Chem.*, 2010, **20**, 8411.
26 B. Minaev, G. Baryshnikov and H. Agren, *Phys. Chem. Chem. Phys.*, 2014, **16**, 1719.
27 X. Yang, J. Loos, S. C. Veenstra, W. J. H. Verhees, M. M. Wienk, J. M. Kroon, M. A. J. Michels and R. A. J. Janssen, *Nano Lett.*, 2005, **5**(4), 579.
28 A. Swinnen, I. Haeldermans, M. V. Ven, J. D'Haen, G. Vanhoyland, S. Aresu, M. D'Olieslaeger and J. Manca, *Adv. Funct. Mater.*, 2006, **16**, 760.
29 X.-T. Hao, L. M. Hirvonen and T. A. Smith, *Methods Appl. Fluoresc.*, 2013, **1**, 015004.
30 C. L. Lee, K. B. Lee and J. J. Kim, *Appl. Phys. Lett.*, 2000, **77**, 2280.
31 A. Bruno, A. D. G. D. Mauro, G. Nenna, M. G. Maglione, S. A. Haque and C. Minarini, *J. Photonics Energy*, 2013, **3**, 033599.
32 M.-R. Choi, T.-H. Han, K.-G. Lim, S.-H. Woo, D. H. Huh and T.-W. Lee, *Angew. Chem., Int. Ed.*, 2011, **50**, 6274.
33 T.-H. Han, Y. B. Lee, M.-R. Choi, S.-H. Woo, S.-H. Bae, B. H. Hong, J.-H. Ahn and T.-W. Lee, *Nat. Photonics*, 2012, **6**, 105.
34 T.-W. Lee, Y. Chung, O. Kwon and J.-J. Park, *Adv. Funct. Mater.*, 2007, **17**, 390.
35 Y.-H. Kim, H. Cho, J. H. Heo, T.-S. Kim, N. Myoung, C.-L. Lee, S. H. Lim and T.-W. Lee, *Adv. Mater.*, 2015, **27**, 7.
36 H. Tanaka and T. Araki, *Chem. Eng. Sci.*, 2006, **61**, 2108.
37 X. Zhang, F. Dou and H. Liu, *J. Polym. Sci., Part B: Polym. Phys.*, 2013, **51**, 749.
38 Y. Liu, G. Zhan, X. Zhong, Y. Yu and W. Gan, *Liq. Cryst.*, 2011, **38**, 995.
39 T. Salim, J. Y. Lek, B. Brauer, D. Fichou and Y. M. Lam, *Phys. Chem. Chem. Phys.*, 2014, **16**, 23829.
40 F. C. Chen, S. C. Chang, G. He, S. Pyo, Y. Yang, M. Kurotaki and J. Kido, *J. Polym. Sci., Part B: Polym. Phys.*, 2003, **41**, 2681.
41 Y. Y. Noh, C. L. Lee and J. J. Kim, *J. Chem. Phys.*, 2003, **118**(6), 2853.
42 N. R. Jung, E. J. Lee, J. H. Kim, H. G. Park, K. M. Park and Y. J. Kang, *Bull. Korean Chem. Soc.*, 2012, **33**(1), 183.